ADVANCED MATERIALS
www.advmat.de

Long-Range Cation Disorder Enhances Comprehensive Performance in Mn-Rich Layered Sodium Cathodes

Maolin Yang, Tingting Yang, Mingjie Dong, Zhongyuan Huang, Yuguang Pu, Lei Jin, Rui Wang, Yuxi Luo, Tao Zeng, Yonglin Tang, Jun Chen, Rafal E. Dunin-Borkowski, Ziwei Chen, Yu Qiao, and Yinguo Xiao**

Mn-rich layered oxides (MRLOs) are promising low-cost cathode materials for sustainable sodium-ion batteries (SIBs). However, the low Mn^{4+}/Mn^{3+} redox potential limits their energy densities, and the Jahn-Teller distortion that occurs surrounding Mn^{3+} at low voltages destabilizes the structure. Additionally, complex ordered structures inherently present in MRLOs hinder Na^+ migration. In this study, new types of cation ordering structures are discovered in common MRLOs. By regulating oxygen vacancy formation, the transition from short-range to long-range cation ordering is disrupted, effectively mitigating cooperative Jahn-Teller distortion and achieving a 95.3% capacity retention over 1 000 cycles at 8 C. The maximum entropy method (MEM) analysis is performed based on neutron diffraction data, which visualizes significantly optimized Na^+ diffusion pathways in long-range disordered cathode with enhanced Na^+ diffusion kinetics. Furthermore, the formation of oxygen vacancy elevates the Mn^{4+}/Mn^{3+} redox potential, resulting in a competitive energy density of 626 Wh kg^{-1} within 1.5–4.5 V in a half-cell configuration. This work offers a multiscale approach to precise elucidation of the cathode crystal structure and provides a feasible pathway to optimize sodium-ion cathodes by disrupting long-range cation ordering, ultimately facilitating substantial improvements in electrochemical performance.

1. Introduction

With the continuous evolution of sustainable clean energy technologies, effective energy storage has become increasingly essential.[1] However, the further market expansion of mainstream lithium-ion batteries (LIBs) is facing limitations including finite resources and high costs. All these challenges create a reasonable opportunity for developing more sustainable large-scale energy storage devices.[2] These alternative solutions are urgently needed to meet the rapidly growing energy storage demands. Among the promising options, sodium-ion batteries (SIBs) have emerged as strong candidates in the sustainable energy storage due to their cost advantages and competitive electrochemical performance.[3]

Akin to LIBs, the cathode material plays a pivotal role in SIBs.[4] Among various cathode materials, manganese-rich layered oxides (MRLOs) have garnered significant interest for their comprehensive performance and cost-effectiveness.[5] Generally, MRLOs can be categorized into two types (that is, P2 and O3) depending on their coordination environments of sodium ions and stacking forms of transition metal (TM) layers.[6] Sodium ions occupy spacious prismatic sites in P2-type structures, which contributes to more facilitated Na^+ diffusion kinetics than that of O3-type cathodes. Despite these merits, state-of-the-art P2-type MRLOs can barely meet the demand for high-power applications.[7] Additionally, the low redox potential of the Mn^{4+}/Mn^{3+} couple results in low energy density.[8] Compounding these challenges, the presence of ordered structures in

---

M. Yang, T. Yang, M. Dong, Z. Huang, Y. Pu, Y. Luo, T. Zeng, Z. Chen, Y. Xiao
School of Advanced Materials
Peking University Shenzhen Graduate School
Peking University
Shenzhen 518055, China
E-mail: chenziwei@zju.edu.cn; y.xiao@pku.edu.cn

J. Chen, Z. Chen
Institute of Zhejiang University-Quzhou
Quzhou 324000, China

T. Yang, L. Jin, R. E. Dunin-Borkowski
Ernst Ruska-Centre for Microscopy and Spectroscopy with Electrons
Forschungszentrum Jülich GmbH
52428 Jülich, Germany

R. Wang
Department of Engineering
University of Cambridge
Cambridge CB30FS, UK

Y. Tang, Y. Qiao
State Key Laboratory of Physical Chemistry of Solid Surfaces
iChEM (Collaborative Innovation Center of Chemistry for Energy Materials)
Department of Chemistry
College of Chemistry and Chemical Engineering
Xiamen University
Xiamen 361005, China

The ORCID identification number(s) for the author(s) of this article can be found under https://doi.org/10.1002/adma.202500984

DOI: 10.1002/adma.202500984

MRLOs, including Na-vacancy[9] and various cation ordering,[10] retards Na^+ diffusion, meanwhile, limits the insertion/extraction capacity of sodium ions and the redox activity of TMs. For instance, House et al. demonstrated that honeycomb-ordered $Na_{0.75}[Li_{0.25}Mn_{0.75}]O_2$ and ribbon-ordered $Na_{0.6}[Li_{0.2}Mn_{0.8}]O_2$ exhibited inferior cation redox activity in the 2–4.5 V range.[10a] Most TM-Mn ordered structures, however, can only be distinguished by neutron diffraction, unless they feature significant atomic number differences, such as Li-Mn and Mg-Mn.[10c,11] Notably, neutron diffraction data of some MRLOs from previous works exhibit peaks indicative of TM-Mn ordering, which are often overlooked, suggesting that cation ordering may be prevalent in MRLOs.[12] Such long-range ordered structures exacerbate the cooperative Jahn-Teller distortion of Mn^{3+}, especially in low voltage regions, accelerating structural degradation.[13] Tremendous efforts have been dedicated to disrupting the ordered cationic arrangements within TM layers by exploiting elemental doping and high entropy strategies,[10c,14] substantial challenges persist. This is largely due to the intricacies of the driving force of such cation ordering. Specifically, the mechanisms of the cation ordering in both long- and short-range structures remain elusive, as well as their impacts on the electrochemical performance of MRLOs.[15]

In this work, we study a series of MRLO cathode materials with progressively increasing dopant concentrations. It should be noted that we adopt sustainable doping element—Fe, in this study. In addition, considering the beneficial effects of Cu doping on the structural and air stability of MRLOs, all synthesized samples were doped with 10% Cu in the TM layer.[16] The impact of temperature on material structures was investigated using high-temperature (HT) neutron diffraction. The results indicate the dependence of long-range cation ordering on annealing temperature. Further analyses, including Rietveld refinement against neutron powder diffraction (NPD) patterns, electron paramagnetic resonance (EPR), and X-ray photoelectron spectroscopy (XPS), unanimously revealed an inverse relationship between the degree of long-range cation order and the concentration of annealing-introduced oxygen vacancy. Moreover, theoretical calculations suggested that bulk oxygen vacancies could elevate the Mn^{4+}/Mn^{3+} redox potential, achieving a competitive energy density of 455 Wh kg^{-1} within 2–4 V. Additionally, maximum entropy method (MEM) simulations based on neutron diffraction data illustrated differences in Na^+ migration paths between ordered and disordered samples. Concretely, the aggregation of Na^+ at specific Na sites in ordered samples impedes the formation of diffusion pathways with adjacent Na sites.

Neutron Pair Distribution Function (nPDF) demonstrated that modified samples retained short-range cation ordering, but the introduction of oxygen vacancies effectively prevented further propagation of cation ordering throughout the lattice. The disruption of cooperative Jahn-Teller distortion surrounding Mn^{3+} leads to reduced lattice strain even at higher sodiated states. Overall, we employed multiscale structural analysis to corroborate that adjusting annealing methods can suppress the expansion of short-range cation ordering into long-range ordering, thereby improving the energy density and cyclability of MRLOs and, meanwhile optimizing Na^+ diffusion pathways.

2. Results and Discussion

2.1. Structure Analysis of As-Synthesized Samples

A series of TM layered oxides, i.e., $Na_{0.67}Mn_{0.9-x}Fe_xCu_{0.1}O_2$ (x = 0.1, 0.2, 0.3), were synthesized using a conventional solid-state method. The products are denoted as 811-O (x = 0.1), 721-O (x = 0.2), and 631-O (x = 0.3) depending on the content of Fe. As shown in Figure S1 (Supporting Information), XRD patterns of all synthesized samples can be indexed to a P2-phase layered structure without any impurities. SEM images (Figure S2, Supporting Information) show a typical micron-scale lamellar morphology for all samples. However, variations in XRD peak intensities suggest some appreciable differences in their crystal structures. Thanks to the non-linear correlation between neutron scattering length and atomic number, Neutron diffraction is a powerful method to distinguish adjacent TMs. In this light, we employed NPD to perform accurate structural analysis. The characteristic peak at d ≈4.03 Å in 811-O indicates a honeycomb-like superstructure in TM layers, which has commonly been observed in reported structures such as $Li@Mn_6$, $Ni@Mn_6$, and $Mg@Mn_6$ (**Figure 1a**).[10] The presence of this peak indicates a new superstructure with cation ordering forms within 811-O. Rietveld refinement results in Figure 1a suggest a satisfactory fit of this new honeycomb superstructure to a $P6_3$ symmetry of $Fe@Mn_6$ and $Cu@Mn_6$ units. Furthermore, the corresponding modified samples were synthesized by adjusting the annealing process and are denoted as 811-D, 721-D, and 631-D, respectively. The ICP-OES results in Table S7 (Supporting Information) indicate that the chemical compositions of the samples are generally consistent with the designed ratios. The XRD patterns and SEM images of modified samples are displayed in Figures S3 and S4 (Supporting Information), respectively. In contrast to 811-O, the NPD patterns of 811-D sample (Figure 1b) do not show any characteristic peak of cation ordering. As shown in Figure 1c, the samples with cation ordering exhibit a $TM@Mn_6$ (TM = Fe or Cu) superstructure in corresponding TM layer. The presence of this superstructure changes the Na_f site (the Na sites sharing faces with TMO_6 octahedrons, while Na_e site-centered polyhedrons share edges with TMO_6 octahedrons) from one in the disordered phase to three in the ordered phase, which inevitably affects Na^+ diffusion behavior.[17] The TM ionic sites in this honeycomb superstructure can be categorized into three different types, namely, TM_{2a}, TM_{2b1}, and TM_{2b2}. The TM_{2b1} site is the center of the honeycomb superstructure, meaning that a higher proportion of Cu or Fe occupying the TM_{2b1} site corresponds to a higher degree of order in the TM layer. As shown in the inset of the Figure S5 (Supporting Information), The TM_{2a} and TM_{2b2} sites correspond to two pairs of equiv. positions on the periphery of the honeycomb superstructure.[10c] Herein, a parameter $DoO(TM@Mn_6)$ can be proposed to quantify the degree of cation ordering in the TM layer, which can be defined as:

$$\mathrm{DoO}\left(\mathrm{TM@Mn_6}\right) = \frac{\mathrm{Occ.}\,(\mathrm{TM, 2b1})}{\mathrm{Occ.}\,(\mathrm{TM, 2a}) + \mathrm{Occ.}\,(\mathrm{TM, 2b1}) + \mathrm{Occ.}\,(\mathrm{TM, 2b2})} \times 100\% \quad (1)$$

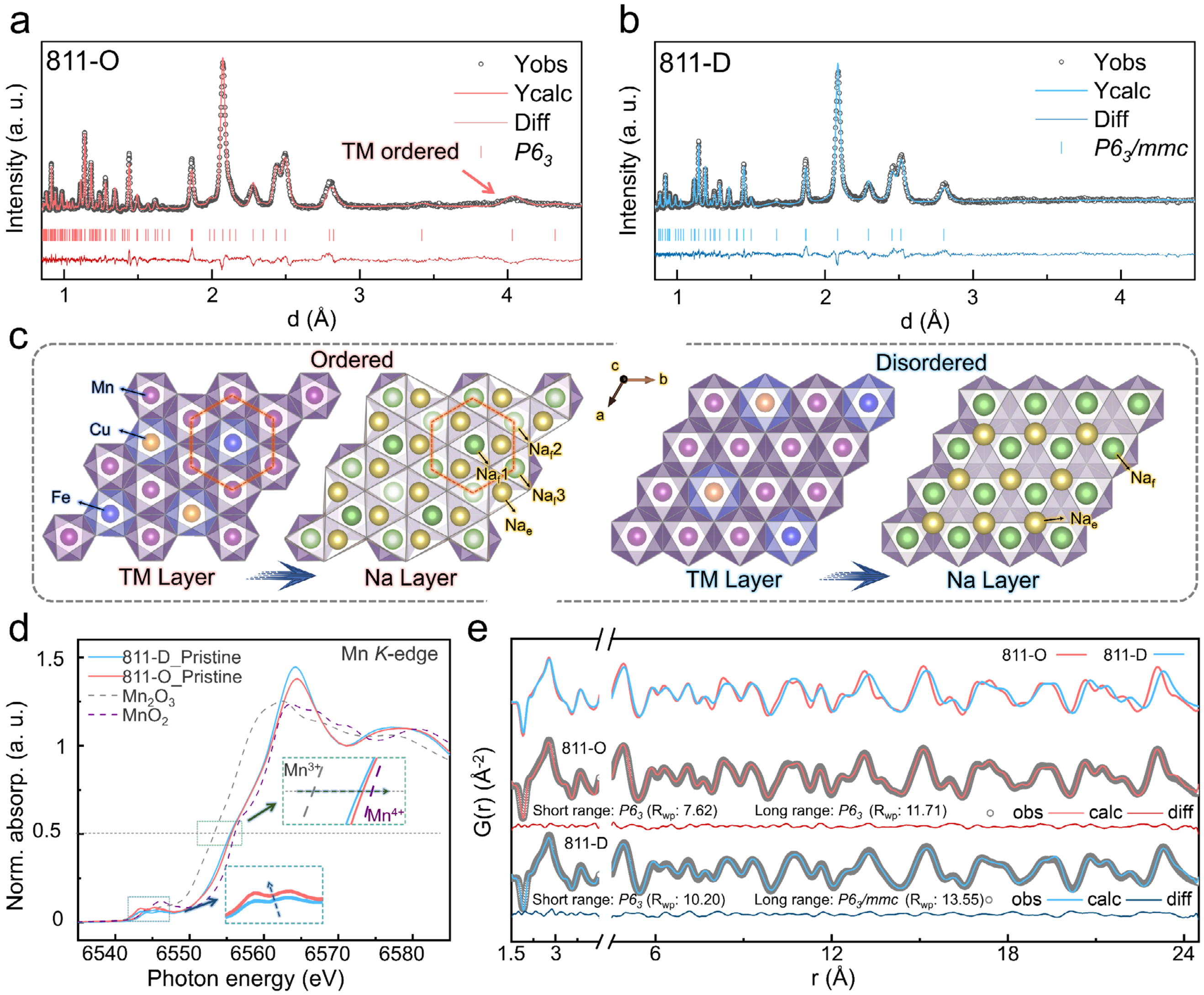

Figure 1. The initial long-range and short-range structures of as-synthesized samples. Rietveld NPD refinement results of 811-O a) and 811-D b); c) Crystal structure schematics with TM ordered and disordered arrangement along [001] zone axis; d) Normalized Mn *K*-edge XANES spectra of 811-O, 811-D and the corresponding standard oxide samples; e) Refinement results of nPDF for 811-O within short-range with $P6_3$ symmetry and long-range with $P6_3$ symmetry; f) Refinement results of nPDF for 811-D within short-range with $P6_3$ symmetry and long-range with $P6_3/mmc$ symmetry.

Figure S5 (Supporting Information) shows the calculated DoO(TM@Mn_6) based on the refinement results for as-synthesized samples (Figure S6a–d, Supporting Information). According to the Equation (1), the closer this value is to 33%, the more disordered the sample is. Conversely, the closer this value is to 100%, the more ordered the TM layer is. It shows nearly disordered arrangement for 811-D and significant ordering for 811-O (Figure S5, Supporting Information). Therefore, 811-O and 811-D were selected as the primary research targets for this study. In addition, increasing Fe content leads to decreased cation ordering. As indicated in the refinement results shown in Tables S1–6 (Supporting Information), the variation of cation ordering may be related to the concentration of oxygen vacancy. The higher oxygen vacancy concentration refers to a lower cation order degree. Furthermore, X-ray absorption spectroscopy (XAS) was carried out to analyze the electronic structure of the samples. Normalized Mn *K*-edge XANES spectra (Figure 1d) indicate that 811-D exhibits lower Mn valence, which is corresponding to its higher concentration of O vacancies. Additionally, the weaker pre-edge peaks for 811-D corresponding to fewer stacking faults, which are detrimental to structural stability during electrochemical cycling.[18] Fe and Cu *K*-edge XANES spectra of both samples (Figure S7, Supporting Information) show similar initial valence states for Fe and Cu.

The above analyses are based on their long-range structures so that further investigation of the short-range structure is necessary to better understand their true structural arrangements. Therefore, nPDF analysis was conducted to extract short-range structural information. As demonstrated in Figure 1e and Figure S8 (Supporting Information), 811-O exhibits cation ordering in both short-range and long-range structures. Despite showing a disordered structure in neutron diffraction, 811-D displays ordered cation arrangement in the short-range region (r = 1.5–4.5 Å, Figure 1e). For the long-range region (r = 4.5–25 Å), the fitting results are consistent with NPD, indicating that the short-range ordering is disrupted in 811-D (Figure 1e; Figure S9, Supporting Information). This long-range ordering will affect Na^+ diffusion kinetics and induce cooperative Jahn-Teller distortions in Mn-based layered oxides, significantly impacting the electrochemical performance.[19]

A detailed microstructure analysis of as-synthesized samples was further conducted. Figure S10a (Supporting Information) presents a high-resolution atomic HAADF-STEM image of 811-D along the [100] zone axis, revealing a clear layered structure. Unfortunately, stacking faults along the interlayer direction are often unavoidable in typical layered cathode materials.[20] Therefore, the large view field within the low-magnification STEM image of 811-O in Figure S11a,b (Supporting Information) displays clear stacking faults, which will tend to propagate during subsequent electrochemical processes, leading to interlayer cracking and failure of the layered cathode.[21] The 811-D with significantly decreasing *DoO*(TM@Mn_6), reduces the cooperative effects in the crystal structure, effectively suppressing the formation of stacking faults (Figure S11c,d, Supporting Information). Due to the similar atomic numbers of Cu, Fe, and Mn, it is hard to determine their specific sites based on contrast differences in high-resolution atomic images along the [001] zone axis (Figure S10b, Supporting Information). However, cation-ordered superstructures, characterized by new periodic TM ions arrangements, can be distinguished through electron diffraction.[19] As shown in Figure S12a,b (Supporting Information), simulated electron diffraction pattern of cation-ordered sample exhibits new periodic diffraction spots that differ from that of disordered sample. This simulation aligns with experimental results, confirming the presence of the TM@Mn_6 superstructure in 811-O (**Figure 2**a,b).

Although the above discussion has clearly confirmed the presence of long-range cation ordering in 811-O, its formation mechanism remains unclear. Motivated by the Rietveld refinement results based on NPD, which reveal a negative correlation between oxygen vacancy concentration and *DoO*(TM@Mn_6), a detailed investigation of the oxygen framework structure is also crucial. EPR is a widely utilized technique for exploring oxygen vacancies in cathode materials.[22] As depicted in Figure 2c, compared to 811-O, 811-D exhibits a much stronger oxygen vacancy signal at $g = 2.003$. The EPR spectra also confirm that the *DoO*(TM@Mn_6) of samples is negatively correlated with the concentration of oxygen vacancies. To explore the spatial distribution of oxygen states in more detail, O *K*-edge EELS spectra were obtained from different regions within the bulk of 811-O and 811-D. As shown in Figure 2d–g, the first peak, located at ≈530 eV (the pre-peak), is associated with electron transitions from the *1s* core level to unoccupied *2p* orbitals that are hybridized with the *3d* metal states. The second peak, around 542 eV (the main peak), corresponds to electron transitions from the *1s* core level to hybridized O *2p* and metal *4sp* orbitals.[24] To ensure consistency, each spectrum was normalized to the intensity of the main peak. In the bulk regions, 811-D consistently shows a lower pre-peak intensity compared to 811-O, indicating a higher concentration of oxygen vacancies in 811-D (Figure 2e,g). These results suggest that controlling oxygen vacancy concentration can reduce the *DoO*(TM@Mn_6). In addition, experiments conducted by Dahn group indicate that during the cooling process of cathode materials from the calcination temperature to room temperature, there is a stage where oxygen is absorbed.[25] This process can eliminate oxygen vacancies formed during HT sintering.[26] Inspired by these findings, this work simulated the synthesis process of 811-O and similarly observed a weight gain during the cooling stage through thermogravimetric analysis (TGA), confirming the elimination of oxygen vacancies in 811-O (Figure S13, Supporting Information). In contrast, for 811-D, the rapid air cooling process limits the diffusion of oxygen into the crystal lattice, thereby preserving the oxygen vacancies formed at high temperatures. The etched O *1s* XPS results in Figure 2h also confirm a negative correlation between the *DoO*(TM@Mn_6) and the concentration of oxygen vacancies in the bulk (Figure S14, Supporting Information).[23] These results further support the notion that the air cooling step facilitates the retention of oxygen vacancies in the bulk. The presence of oxygen vacancies drives a partial reduction of Mn^{4+} to Mn^{3+} to maintain overall charge neutrality (Figure 1d). Furthermore, since the ionic radius of Mn^{3+} is more comparable to those of Fe^{3+} and Cu^{2+} than that of Mn^{4+}, a more uniform and random distribution of cations within the TM layer is favored,[15a] thereby reducing the *DoO*(TM@Mn_6).

To further substantiate that oxygen vacancies promote cation disordering, this work designed a TGA-MS (Mass Spectrometry) experiment on the 811-O sample. A significant weight loss was observed in Figure 2i when it was heated to ≈400 °C, accompanied by the release of oxygen. Subsequently, HT-NPD experiments revealed that the cation disorder in the TM layer was eliminated right after oxygen release (Figure S15, Supporting Information). These results confirm that the formation of oxygen vacancies promotes cation disorder in the TM layer. This implies that artificially generating or preserving oxygen vacancies formed during the calcination process can effectively reduce the *DoO*(TM@Mn_6).

2.2. Electrochemical Performance and Charge Compensation Mechanism

To investigate the impact of cation disorder on the electrochemical performance of cathode materials, a series of electrochemical characterizations were conducted. It should be noted that all the following electrochemical characterizations were tested in half-cells assembled with a metallic sodium anode. **Figure 3**a shows the initial galvanostatic charge discharge (GCD) curves of 811-O and 811-D at 0.1C within a voltage range of 1.5–4.5 V. The curves exhibit significant differences in shape, particularly in discharge capacity, with 811-D demonstrating a discharge specific capacity ≈32 mAh g^{-1} higher than that of 811-O. Further differential analysis of the first and second GCD curves reveals the dQ dV^{-1} plots in the inset of Figure 3a. The 811-D sample exhibits a significantly enhanced Mn^{4+}/Mn^{3+} redox couple (2.21 V/2.11 V vs Na^+/Na), indicating higher cation redox activity in the disordered sample. Notably, both samples show plateaus above 4.0 V related to phase transitions and oxygen redox reactions, which are detrimental to prolonged electrochemical cycling.[11] Furthermore, Galvanostatic Intermittent Titration Technique (GITT) tests within 1.5–4.5 V reveal that both samples exhibit significant kinetic hysteresis above 4.0 V, with the Na^+ diffusion coef-

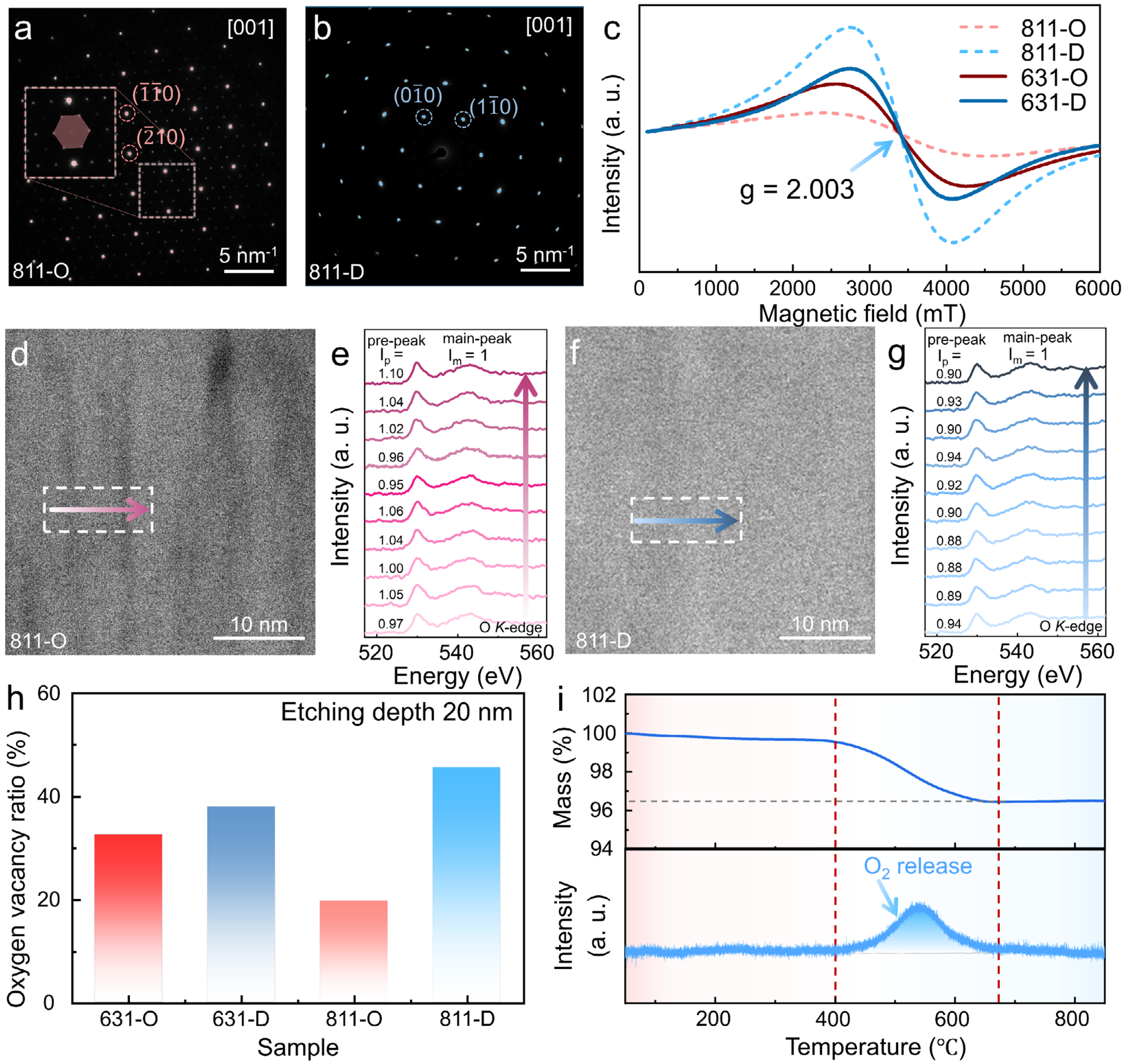

Figure 2. The initial oxygen structures of as-synthesized samples. SAED images of 811-O a) and 811-D b) along [001] zone axis. Inset of (a) is the enlarged image of the rectangle region; c) EPR spectra of as-synthesized samples at initial state; d) STEM-HAADF image of 811-O; e) O *K*-edge EELS spectra acquired along the trajectory marked by the arrows inside the dashed box in (d); f) STEM-HAADF image of 811-D; g) O *K*-edge EELS spectra acquired along the trajectory marked by the arrows inside the dashed box in (f). h) The calculated oxygen vacancy radios of as synthetized samples base on their integral area in O *1s* XPS spectra; i) In situ TGA-MS measurement of 811-O during heating process.

ficient (D_{Na^+}) dropping by two orders of magnitude (Figure S16, Supporting Information). Furthermore, both samples exhibit extremely limited capacity in the 1.5–2 V (Figure 3a), which, however, increases the risk of structural distortion and electrolyte decomposition over a wider voltage window.[26] Therefore, to avoid the complex factors of structural distortion, phase transitions and oxygen redox reactions while ensuring substantial capacity, this study focuses on the voltage window within 2–4 V. As shown in Figure 3b, 811-D delivers a reversible discharge specific capacity of ≈181 mAh g^{-1} within 2–4 V, 40 mAh g^{-1} higher than 811-O. This difference is comparable to that observed in the 1.5–4.5 V, indicating that the impact of ordering on the charge compensation mechanism is primarily due to differences in cation redox activity. The dQ dV^{-1} plots within 2–4 V also exhibit significantly enhanced Mn^{4+}/Mn^{3+} redox peaks for 811-D in Figure 3c.

Further, hard XAS was used to analyze the charge compensation mechanisms of 811-O and 811-D. As shown in Figures S17 and 18 (Supporting Information), 811-D exhibits higher Mn redox activity, achieving reversible transitions between Mn$^{3.85+}$ and Mn$^{3.01+}$.[19] In contrast, 811-O can only change valence within

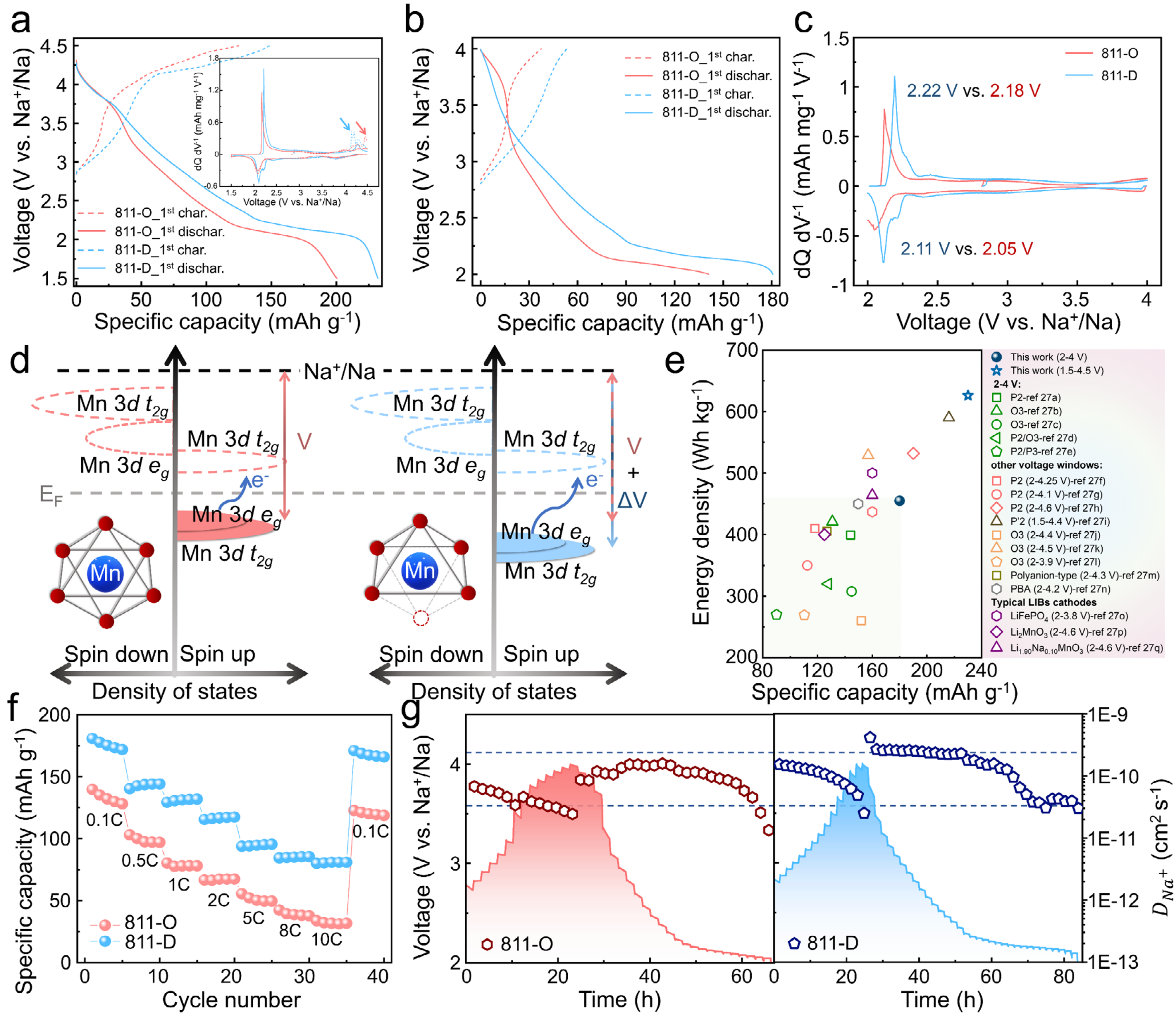

Figure 3. Electrochemical performance and charge compensation mechanism. a) Typical GCD curves of 811-O and 811-D during the first cycle within 1.5–4.5 V; The inset shows the dQ dV^{-1} curves derived from the differential analysis of their first two GCD cycles; Typical GCD curves b) and the dQ dV^{-1} curves c) of 811-O and 811-D during the first cycle within 2–4 V; d) Schematic band diagrams derived from projected DOS of the Mn *3d* orbitals in 811-O and 811-D. The bottom part is the *3d* orbital electronic configurations of Mn^{3+} and Mn^{4+}; e) A comparison chart is presented between the performance of 811-D and other representative SIBs cathodes as well as typical LIBs cathodes. The x-axis represents specific capacity, while the y-axis depicts energy density. All data presented in the figure were collected in a half-cell configuration[26,27]; f) The rate performance comparation of 811-O and 811-D at various rates; g) GITT curves of 811-O and 811-D at initial cycle within 2–4 V, and corresponding D_{Na^+} calculated via GITT tests.

$Mn^{3.93+}$ and $Mn^{3.73+}$, which significantly impacts the capacity of Mn-rich cathodes (Figures S17 and 18, Supporting Information). Furthermore, the etched Mn *2p* XPS results shown in Figure S19 (Supporting Information) corroborate the XAS results, indicating enhanced Mn^{4+}/Mn^{3+} redox activity in 811-D. The Cu and Fe valence variation trends are similar for both samples (Figure S20, Supporting Information). Electrochemical tests on 721-D and 631-D further support the enhancement of cation redox activity (particularly for Mn) due to cation disorder (Figure S21, Supporting Information). Beyond specific capacity, redox voltage significantly influences energy density. Notably, in Figure 3c, 811-D shows a higher Mn redox voltage (2.22/2.11 V vs 2.18/2.05 V for 811-O), which is advantageous for improving the energy density of Mn-rich layered cathodes. The elevated Mn redox voltage in 811-D is closely associated with bulk oxygen vacancies. Figure S22a,b (Supporting Information) compares the electronic structures of Mn *3d* orbitals in 811-O and 811-D through density of states (DOS) analysis, with schematic band diagrams presented in Figure 3d. The Mn *3d eg* states (spin-up) split into occupied states in the valence band and unoccupied states in the conduction band. As cation disorder increases, the energy of the occupied Mn *3d eg* states shifts farther from the Fermi level, widening the energy gap between the Mn redox states and the Na^+/Na reference (Figure S22, Supporting Information). This shift is primarily caused by the presence of oxygen vacancies, which reduce the local symmetry of the Mn-O ligands from a cubic or tetragonal arrangement. This symmetry reduction induces local orbital coupling, lowering the energy level of the Mn *3d* orbitals, which contributes to the elevated redox voltage.[18] Benefiting from the enhanced cation redox activity and the elevated Mn^{4+}/Mn^{3+} redox voltage due to oxygen vacancy, the 811-D cathode exhibits highly competitive energy density. Within a voltage range of 2–4 V, it achieves an energy density of 455 Wh kg^{-1}, surpassing most reported layered SIBs cathode materials in the same voltage window (Figure 3e). Furthermore, in the broader voltage range of 1.5–4.5 V, the energy density of 811-D reaches an impressive 626 Wh kg^{-1}, outperforming the majority of reported SIBs cathode materials and even rivaling some benchmark lithium-ion cathode materials such as $LiFePO_4$ and Li_2MnO_3. Furthermore, full cells were assembled by pairing the cathodes with hard carbon (HC). As shown in Figure S23 (Supporting Information), at 1C and within a voltage window of 1.9–3.9 V (vs HC, since HC has a potential of ≈0.1 V vs Na^+/Na), the 811-D||HC delivers an energy density of 333 Wh kg^{-1}, which is significantly higher than the 275 Wh kg^{-1} achieved by 811-O||HC. These results highlight 811-D's exceptional potential for practical applications. In addition, long-term cycling performance tests were conducted. As shown in Figures 24 and 25 (Supporting Information), 811-D delivers a reversible specific capacity of 140 mAh g^{-1} at 1C within 2–4 V, with a capacity retention of 87% over 100 cycles, significantly higher than the control groups. In situ XRD analyses of both samples were conducted to elucidate the superior cycling stability of 811-D observed in the long-cycle tests (Figure S26, Supporting Information). Benefiting from the cation disordering on structural evolution, 811-D exhibits structural strain comparable to or even lower than that of 811-O, thereby enhancing its cycling stability. At the rate of 8C, 811-D maintains a capacity retention of 95.3% compared to the 64.1% of 811-O after 1 000 cycles, further demonstrating the significant enhancement in structural stability due to cation disorder (Figure S27, Supporting Information). In addition, cation disordering also effectively enhances the air stability of the electrodes, which is regarded as one of the core issues for SIB cathodes in practical applications (Figure S28, Supporting Information).

Moreover, the cation ordering within the TM layers alters the Na^+ occupancy sites in the Na layers, which significantly impacts Na^+ diffusion behavior. As illustrated in Figure 3f, 811-D delivers a discharge capacity of 81 mAh g^{-1} at a 10C rate, while 811-O only achieves 32 mAh g^{-1}. This enhanced rate capability indicates that the cation disorder has improved Na^+ diffusion kinetics. Additionally, GITT analysis reveals that 811-D maintains a D_{Na^+} ≈5 times higher than that of 811-O throughout the charge-discharge cycles (Figure 3g). In contrast, 631-D shows similar D_{Na^+} values to 631-O (Figure S29a,b, Supporting Information), further confirming that the kinetic optimization arises from cation disorder. The following analyses will delve deeper into how cation disorder influences Na^+ diffusion dynamics.

2.3. Optimized Mechanism of Na+ Diffusion

Based on the electrochemical results, despite 811-D inserting and extracting more Na^+ (≈0.16 mol) compared to 811-O, it still demonstrates superior Na^+ diffusion kinetics. Moreover, there are differences between their crystal structures, attributed to the reduced symmetry caused by cation ordering, resulting in the Wyckoff position within the TM layer dispersing from a single *2a* site to three sites (*2b1*, *2b2*, and *2a*). Similarly, the Wyckoff position of Na_f, initially at the *2b* site is dispersed to the *2b1*, *2b2*, and *2a* sites (labeled as Na_f1, Na_f2 and Na_f3, respectively). This undoubtedly affects the Na^+ diffusion pathways.

The MEM is considered a reliable approach for evaluating 3D scattering densities from finite information by maximizing information entropy under constraints.[28] Herein, the nuclear distribution of sodium was calculated by MEM using room-temperature NPD data, which can be used to visualize the possible Na^+ diffusion paths.[15a] As illustrated in **Figure** 4a,b, positive nuclear density maps can describe the probable Na^+ migration pathway for 811-D due to the positive neutron scattering length of Na^+. Since the NPD data were measured at room temperature, the nuclear density distribution of sodium is mainly concentrated at its initial sites, but connectivity pathways between different Na^+ sites within the disordered phase can still be observed. As shown in Figure 4b, Na^+ migration between adjacent Na_e and Na_f prismatic sites might not pass through the face center of the shared face but rather occurs at about one-third of the distance from the prismatic edge. Similarly, MEM simulated the Na^+ diffusion path for 811-O (Figure 4c,d). Due to the presence of the TM@Mn_6 superstructure, the Na^+ at the Na_e sites is concentrated near the Na_f1 site, significantly reducing the connectivity between the Na_e site and the remaining two Na_f sites (Na_f2 and Na_f3). The lack of connectivity between adjacent Na_e and $Na_f2(3)$ sites corroborates the poorer Na^+ diffusion kinetics in 811-O. To further investigate the impact of cation disorder on Na^+ diffusion, first-principles computations were employed based on density functional theory (DFT) to map Na^+ migration pathways and assess their energy barriers. As illustrated in the inset of Figure 4e and in Figure S30 (Supporting Information), Na^+ diffusion pathways in both 811-D and 811-O were analyzed based on MEM results and optimized DFT models. According to climbing nudged elastic band (cNEB) calculations (Figure 4e), the migration barrier for Na^+ in the 811-D crystal is ≈0.36 eV, whereas for 811-O, this barrier increases to 0.60 eV. This suggests that cation disorder induced by the honeycomb superlattice of the TM layers leads to Na^+ accumulation around the Na_e sites near Na_f1, which obstructs Na^+ connectivity across the 2D planes and impedes diffusion kinetics.

Furthermore, insights from the in situ neutron diffraction experiment on 811-O during heating indicate that examining Na^+ diffusion transitions across varying temperatures can illuminate how cation disorder affects the spatial arrangement of Na^+ sites (Figure 4f). The MEM applied to neutron diffraction data under temperature variation highlights the evolution of Na^+ pathways during the cation disorder transition. Figure 4g depicts the development of positive nuclear scattering density as the ordered cation phase is gradually heated, simulating the transition in Na^+ diffusion paths. It can be observed that as the cation ordering decreases, the positive nuclear scattering density at the Na_e sites gradually diffusion, forming channels with adjacent $Na_f2(3)$ sites. By the end of the heating process (upon 600 °C), the positive nuclear scattering density distribution closely resembles that of the cation-disordered structure. This in situ heated experiment

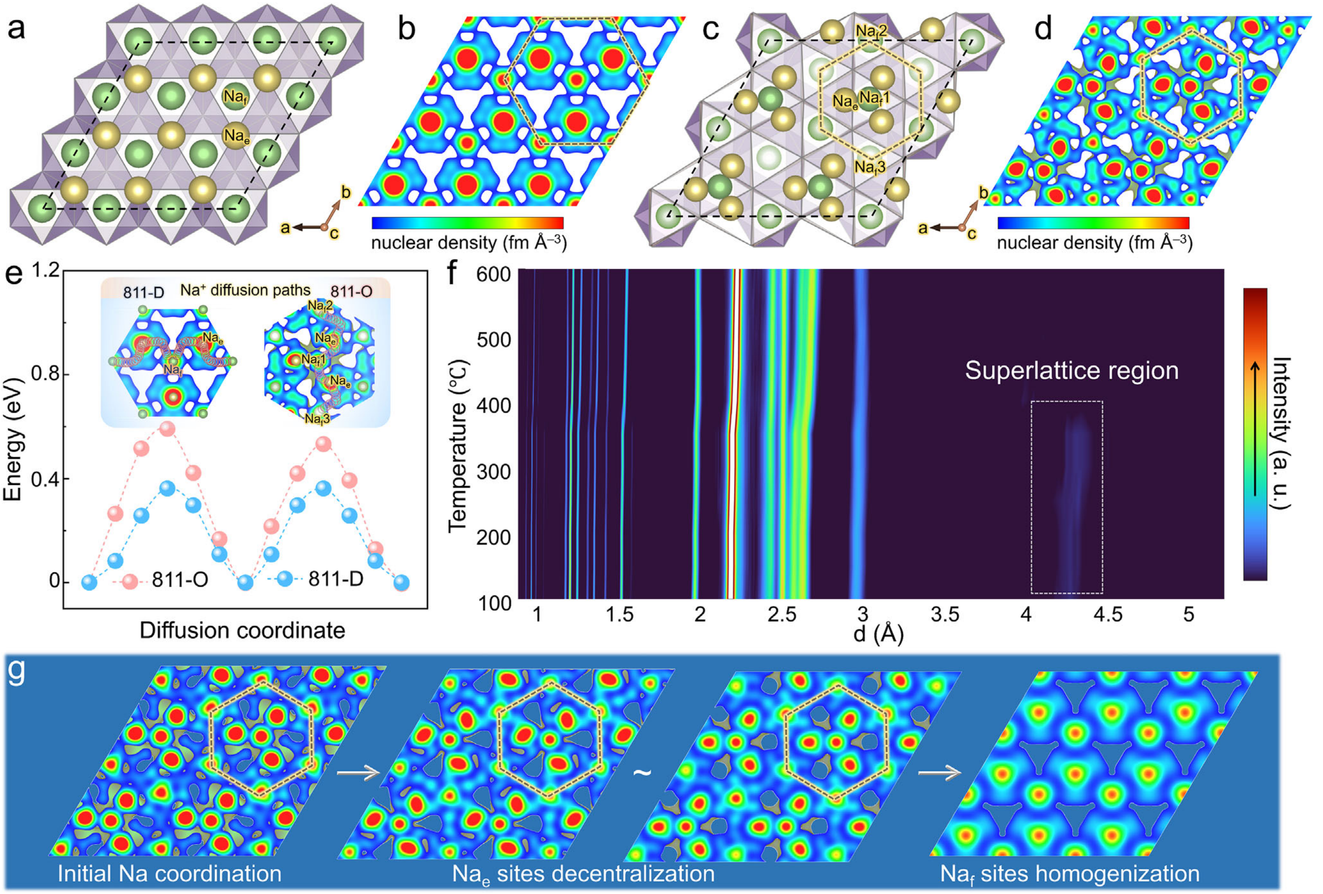

Figure 4. Visualization of Na^+ migration pathways. a) Crystal structure of 811-D with two types of Na^+ sites along the [001] zone axis based on NPD refinement; b) MEM reconstructed positive nuclear density maps of 811-D at pristine state; c) Crystal structure of 811-O with two types of Na^+ sites along the [001] zone axis based on NPD refinement; d) MEM reconstructed positive nuclear density maps of 811-O at pristine state; e) The migration barrier for Na^+ in the 811-D and 811-O base on DFT calculation. Inset is Na^+ diffusion pathways in both 811-D and 811-O based on MEM results and optimized DFT models; f) In situ NPD patterns of 811-O during the heating process; g) MEM reconstructed positive nuclear density maps of 811-O during the heating process.

further verifies that adjusting the annealing process helps maintain the cation-disordered structure at high temperatures, which is beneficial for Na^+ diffusion behavior in layered oxides.

3. Conclusions

Overall, this work discovered a new type of honeycomb long-range cation ordering, TM@Mn_6 (TM = Cu or Fe), in MRLOs. By regulating the annealing process to introduce oxygen vacancy, the degree of this long-range ordering was reduced. Additionally, the introduction of oxygen vacancy lowered the local symmetry of Mn-O ligands from cubic or tetragonal to C_{4v} in the cation-disordered 811-D, resulting in local orbital coupling and enhancing the Mn redox potential. Consequently, 811-D delivers a highly competitive energy density of 626 Wh kg^{-1} within 1.5–4.5 V in a half-cell configuration. Additionally, long-range cation ordering significantly impacts Na^+ diffusion kinetics. Cation ordering reduces crystal symmetry, dispersing the single Na_f site into three distinct Na_f sites. The aggregation of Na^+ at the Na_e site disrupts connectivity with adjacent Na_f sites, hindering Na^+ diffusion and reducing cationic redox activity due to kinetic delays. In situ NPD experiments during heating process further revealed the evolution of Na^+ diffusion pathways from cation-ordered to cation-disordered states, demonstrating the significant influence of cation disordering on Na^+ diffusion. Last, the disruption of the transition from short-range to long-range cation ordering in 811-D reduced the cooperative Jahn-Teller distortion effect at low voltages. This maintained low structural strain despite higher Na^+ (de)insertion compared to 811-O, significantly enhancing structural stability. Consequently, 811-D retained 95.3% capacity after 1 000 cycles at 8C.

By analyzing the formation mechanisms, diffusion pathways, and cationic charge compensation mechanisms in cation-ordered MRLOs, we propose a long-range cation disordering strategy that fundamentally improves the overall electrochemical performance. This strategy holds promise for broad application in the industrial optimization of sodium-ion layered cathodes.

4. Experimental Section

Materials Synthesis: A series of Mn-rich layered oxide (MRLO) materials in this paper were synthesized through regulating the proportion of elements and the annealing process in the solid-state synthesis reaction. Specifically, there are three kinds of slowly cooled materials, $Na_{0.67}Mn_{0.9-x}Fe_xCu_{0.1}O_2$ (where x = 0.1, 0.2, 0.3 and are respectively designated as 811-O, 721-O, 631-O), and three air cooling materials that are respectively designated as 811-D, 721-D, 631-D. Na_2CO_3 (Sinopharm Chemical, 99.8%), Fe_2O_3 (Aladdin, 99.9%), CuO (Sinopharm Chemical, 99%), and Mn_2O_3 (Sinopharm Chemical, 98%) were blended in a high-energy ball mill in accordance with the relevant stoichiometric values. The resultant three types of mixed materials with different element ratios were sintered in a muffle furnace, heated to 900 °C at a rate of 3 °C min^{-1}, then remained at 900 °C for 20 h in air, and finally cooled to room temperature at a rate of 1 °C min^{-1}, thereby obtaining the ordered series materials. In the same manner, the mixed materials with three distinct element ratios were heated to 900 °C, and held for 20 h. The disordered series materials were obtained through directly exposing the HT sintered samples to ambient room-temperature air, thereby achieving air cooling.

Electrochemical Measurement: In this paper, all electrochemical properties were compared and studied through the utilization of coin-type cells (2032). The slurry composed of 80 wt.% active material (as-synthesized cathode materials or HC anode material), 10 wt.% polyvinylidene fluoride (PVDF), 10 wt.% acetylene black, and an appropriate amount of N-methyl-2-pyrrolidone (NMP) was uniformly dispersed on a 10 µm thick aluminum foil to prepare the working electrode. After drying in an oven at 80 °C, the electrode plates were cut into discs with a diameter of 10 mm. The as-prepared cathode electrodes have an active material loading of ≈1.8 mg cm^{-2} and a thickness of ≈10 µm. To balance capacity (with an N/P ratio of ≈2), the anode's active mass loading is maintained at ≈1 mg cm^{-2}, with an additional 10% of HC added to compensate for capacity loss. Furthermore, they were dried in a vacuum oven at 110 °C for 12 h to eliminate all traces of solvent, and then transferred to an argon-filled glove box (Mikrouna Super 1220, H_2O and O_2 < 0.01 ppm) for cell assembly. Sodium foil was employed as the counter electrode, and glass fiber (GB-100R, ADVANTEC Co., Japan) was used as the separator. The 1 M $NaClO_4$ was dissolved in ethylene carbonate/diethyl carbonate (EC/DEC, with a volume ratio of 1:1) and fluoroethylene carbonate (FEC) with a volume ratio of 5% served as the electrolyte. The assembled coin-type half-cells (2 032) were conducted to typical galvanostatic discharge/charge tests in the voltage window of 1.5–4.5 V, 1.5–4.0 V, and 2.0–4.0 V respectively on a Neware Battery Tester. The GCD tests were conducted at a constant temperature of 25 °C. Prior to the long-term cycling test at 1C, an initial activation step at 0.1C was performed. For the long-term cycling test at 8C, a segmented activation process at 1C, 2C, and 5C was implemented to meet the requirements for high-rate testing. During each charge-discharge interval, a 1-min rest period was implemented to reduce electrochemical polarization. Cyclic voltammetry (CV) experiments were carried out using the OCTOSTAT200 electrochemical workstation (IVIUM Instrument). GITT, which at a current rate of 0.1C for 15 min followed by a 90 min rest, was carried out on a Neware Battery Tester. For the diffusion coefficient of Na^+ (D_{Na^+}), which can be calculated using Equation (2),

$$D_{Na}+ = \frac{4}{\pi\tau}\left(\frac{m_B V_M}{M_B S}\right)^2\left(\frac{\Delta E_s}{\Delta E_t}\right)^2\left(t << \frac{L^2}{D_{Na}}\right) \tag{2}$$

where τ represents the duration time of the current pulse (s), m_B is the mass of the active material (g), V_M is the molar volume of the material (cm^3 mol^{-1}), M_B is the molecular weight of the active material (g mol^{-1}), S is the contact area at the interface between the electrolyte and the electrode (cm^2), ΔE_s is the steady-state voltage change, ΔE_t is the total voltage change during the current pulse, L is the diffusion length (cm), and D_{Na^+} is the chemical diffusion coefficient of Na^+ (cm^2 S^{-1}).

Structural Characterization: The exploration of the crystal structures of the samples was carried out through X-ray and neutron diffraction measurements. The X-ray diffraction (XRD) patterns of the powder samples were obtained by the Bruker D8-Discover diffractometer at room temperature with the utilization of Cu Kα radiation. Regarding in situ XRD research, the experiment was conducted on the same XRD diffractometer in combination with the in situ device. The NPD experiment was implemented on the Time-of-Flight (TOF) diffractometer Multi-Physics Instrument (MPI) (https://csns.cn/31113.02.CSNS.MPI) of the China Spallation Neutron Source (CSNS) (https://csns.cn/31113.02.CSNS). Afterward, the Fullprof program was employed to analyze the crystal structures by means of the Rietveld refinement methods. The morphology, atomic-resolution images and elemental distribution of the samples were investigated by means of scanning electron microscope (SEM, ZEISS SUPRA 55), scanning transmission electron microscope (STEM, JEM–3200FS, 300 keV), and energy dispersive spectrometer (EDS, OXFORD, X-MaxN TSR). HT neutron diffraction experiment: HT neutron diffraction experiment was conducted on Wombat, which is a high-intensity neutron diffractometer situated in the OPAL Neutron Guide Hall of Australia. The 811-O was initially heated from room temperature to 100 °C at a rate of 7 °C min^{-1}, and then further heated to 600 °C at a rate of 1 °C min^{-1}. The neutron diffraction data were logged throughout the entire process through continuous data extraction. Synchrotron XAS measurements: The electrodes were disassembled from the coin cells that were charged or discharged to various potentials. Due to its high penetration and low absorption, Synchrotron X-ray accurately reflects the structural properties of the bulk sample, which is advantageous when observing minute phase changes that are typically not discernible in laboratory-scale X-ray diffraction because of poor background noise. The hard X-ray absorption spectroscopy (hXAS) of these samples was carried out on the hard X-ray general spectroscopy beamline (BL11B) of the Shanghai Synchrotron Radiation Facility, Shanghai, China.

DFT Calculations: All the DFT calculations were implemented in the Vienna Ab-initio Simulation Package (VASP)[29] with the projector-augmented method. The electron wave function of valence electrons was expanded using the Projected Augmented Wave (PAW) base set. The Generalized Gradient Approximation (GGA)[30] level of DFT+D3 with the Perdew-Burke-Ernzerhof (PBE)[31] exchange-correlation functional was employed to describe the exchange-correlation effects in this study. The plane wave truncation energy of 520 eV and the system's total energy of less than 1.0×10^{-5} eV were utilized for all the calculations. To describe on-site Coulomb interactions, all elementary reaction steps were calculated using the DFT+U method, with a U value of 3.9 eV for Mn-*3d*, 4.0 eV for Fe-*3d*, 4.0 eV for Cu-*3d*, which was determined using the tetrahedron integration method. The Gamma *k*-point sampling method was carried out for all calculations with $2 \times 2 \times 1$ *k*-point samplings. The cNEB method was utilized to investigate the transition states and migration pathways of lithium ions in the solid solution. In the cNEB framework, a series of images representing the reaction pathway were generated between the two Na-ion sites.

Supporting Information

Supporting Information is available from the Wiley Online Library or from the author.

Acknowledgements

M.Y., T.Y., and M.D. contributed equally to this work. The research was financially supported by the National Key R&D Program of China (2020YFA0406203), National Natural Science Foundation of China (No. 92472115 and No. 52072008), Guangdong Basic and Applied Basic Research Foundation (No. 2022B1515120070, No. 2022A1515110816, and No. 2022A1515110596), and the Large Scientific Facility Open Subject of Songshan Lake, Dongguan, Guangdong (No. KFKT2022A04). The Major Science and Technology Infrastructure Project of Material Genome Big-science Facilities Platform supported by the Municipal Development and Reform Commission of Shenzhen also contributed to this research. The authors appreciate the neutron beamtime at Wombat granted from OPAL Neutron Guide Hall, Australia; Maxim Avdeev for technical assistance during high temperature neutron diffraction experiments; the neutron beamtime at MPI granted from CSNS, Dongguan, China; Yuanguang Xia, Jupjng Xu, and Wen Yin for technical assistance during NPD and nPDF experiments; the hXAS beamtime at BL11B granted from SSRF, Shanghai, China; Jiong Li and Qian Gao for technical assistance during hXAS experiments; and the assistance provided by Bao Qiu in conducting the TGA and TGA-MS measurements.

Conflict of Interest

The authors declare no conflict of interest.

Data Availability Statement

The data that support the findings of this study are available from the corresponding author upon reasonable request.

Keywords

long-range cation disorder, maximum entropy method (MEM), Mn-rich layered oxides (MRLOs), Na$^+$ migration paths, O vacancies

Received: January 14, 2025
Revised: April 10, 2025

---

[1] a) N. Kittner, F. Lill, D. M. Kammen, *Nat. Energy* **2017**, *2*, 17125; b) D. Larcher, J. M. Tarascon, *Nat. Chem.* **2015**, *7*, 19.
[2] a) A. Manthiram, *ACS Cent. Sci.* **2017**, *3*, 1063; b) M. Li, J. Lu, Z. Chen, K. Amine, *Adv. Mater.* **2018**, *30*, 1800561.
[3] a) C. Vaalma, D. Buchholz, M. Weil, S. Passerini, *Nat. Rev. Mater.* **2018**, *3*, 18013; b) N. Yabuuchi, K. Kubota, M. Dahbi, S. Komaba, *Chem. Rev.* **2014**, *114*, 11636; c) P. K. Nayak, L. Yang, W. Brehm, P. Adelhelm, *Angew. Chem., Int. Ed.* **2018**, *57*, 102.
[4] a) J. Liu, J. Wang, Y. Ni, K. Zhang, F. Cheng, J. Chen, *Mater. Today* **2021**, *43*, 132; b) M. H. Han, E. Gonzalo, G. Singh, T. Rojo, *Energy Environ. Sci.* **2015**, *8*, 81.
[5] a) E. Gonzalo, M. Zarrabeitia, N. E. Drewett, J. M. López del Amo, T. Rojo, *Energy Storage Mater.* **2021**, *34*, 682; b) Z. Chen, Y. Deng, J. Kong, W. Fu, C. Liu, T. Jin, L. Jiao, *Adv. Mater.* **2024**, *36*, 2402008.
[6] a) C. Delmas, C. Fouassier, P. Hagenmuller, *Physica B+C (Amsterdam)* **1980**, *99*, 81; b) C. Delmas, J.-J. Braconnier, P. Hagenmuller, *Mater. Res. Bull.* **1982**, *17*, 117.
[7] a) J. Wang, Y.-F. Zhu, Y. Su, J.-X. Guo, S. Chen, H.-K. Liu, S.-X. Dou, S.-L. Chou, Y. Xiao, *Chem. Soc. Rev.* **2024**, *53*, 4230; b) S. Liu, J. Wan, M. Ou, W. Zhang, M. Chang, F. Cheng, Y. Xu, S. Sun, C. Luo, K. Yang, C. Fang, J. Han, *Adv. Energy Mater.* **2023**, *13*, 2203521.
[8] a) N. Yabuuchi, M. Kajiyama, J. Iwatate, H. Nishikawa, S. Hitomi, R. Okuyama, R. Usui, Y. Yamada, S. Komaba, *Nat. Mater.* **2012**, *11*, 512; b) H. Hu, H.-C. He, R.-K. Xie, C. Cheng, T. Yan, C. Chen, D. Sun, T.-S. Chan, J. Wu, L. Zhang, *Nano Energy* **2022**, *99*, 107390.
[9] a) P.-F. Wang, H.-R. Yao, X.-Y. Liu, Y.-X. Yin, J.-N. Zhang, Y. Wen, X. Yu, L. Gu, Y.-G. Guo, *Sci. Adv.* **2018**, *4*, aar6018; b) Y. Liu, C. Wang, S. Zhao, L. Zhang, K. Zhang, F. Li, J. Chen, *Chem. Sci.* **2021**, *12*, 1062.
[10] a) R. A. House, U. Maitra, M. A. Pérez-Osorio, J. G. Lozano, L. Jin, J. W. Somerville, L. C. Duda, A. Nag, A. Walters, K.-J. Zhou, M. R. Roberts, P. G. Bruce, *Nature* **2020**, *577*, 502; b) C. Zhao, Z. Yao, J. Wang, Y. Lu, X. Bai, A. Aspuru-Guzik, L. Chen, Y.-S. Hu, *Chem* **2019**, *5*, 2913; c) Z. Lu, R. A. Donaberger, J. R. Dahn, *Chem. Mater.* **2000**, *12*, 3583.
[11] J. W. Somerville, A. Sobkowiak, N. Tapia-Ruiz, J. Billaud, J. G. Lozano, R. A. House, L. C. Gallington, T. Ericsson, L. Häggström, M. R. Roberts, U. Maitra, P. G. Bruce, *Energy Environ. Sci.* **2019**, *12*, 2223.
[12] a) X. Liu, G. Zhong, Z. Xiao, B. Zheng, W. Zuo, K. Zhou, H. Liu, Z. Liang, Y. Xiang, Z. Chen, G. F. Ortiz, R. Fu, Y. Yang, *Nano Energy* **2020**, *76*, 104997; b) Z. Chen, M. Yang, G. Chen, G. Tang, Z. Huang, M. Chu, R. Qi, S. Li, R. Wang, C. Wang, T. Zhang, J. Zhai, W. Zhao, J. Zhang, J. Chen, L. He, J. Xu, W. Yin, J. Wang, Y. Xiao, *Nano Energy* **2022**, *94*, 106958.
[13] X. Zhu, F. Meng, Q. Zhang, L. Xue, H. Zhu, S. Lan, Q. Liu, J. Zhao, Y. Zhuang, Q. Guo, B. Liu, L. Gu, X. Lu, Y. Ren, H. Xia, *Nat. Sustain.* **2021**, *4*, 392.
[14] B. Ran, H. Li, R. Cheng, Z. Yang, Y. Zhong, Y. Qin, C. Yang, C. Fu, *Adv. Sci.* **2024**, *11*, 2401034.
[15] a) Y. Wang, R. Xiao, Y.-S. Hu, M. Avdeev, L. Chen, *Nat. Commun.* **2015**, *6*, 6954; b) A. Zeng, J. Jiao, H. Zhang, E. Zhao, W. Yin, B. T. Wang, X. Xiao, *Mater. Today Chem.* **2023**, *30*, 101532.
[16] a) W. Zuo, J. Qiu, X. Liu, F. Ren, H. Liu, H. He, C. Luo, J. Li, G. F. Ortiz, H. Duan, J. Liu, M.-S. Wang, Y. Li, R. Fu, Y. Yang, *Nat. Commun.* **2020**, *11*, 3544; b) Y. Yoda, K. Kubota, K. Kuroki, S. Suzuki, K. Yamanaka, T. Yaji, S. Amagasa, Y. Yamada, T. Ohta, S. Komaba, *Small* **2020**, *16*, 2006483; c) J. Xu, J. Chen, K. Zhang, N. Li, L. Tao, C.-P. Wong, *Nano Energy* **2020**, *78*, 105142.
[17] J. Xu, D. H. Lee, R. J. Clément, X. Yu, M. Leskes, A. J. Pell, G. Pintacuda, X.-Q. Yang, C. P. Grey, Y. S. Meng, *Chem. Mater.* **2014**, *26*, 1260.
[18] Q. Li, D. Ning, D. Wong, K. An, Y. Tang, D. Zhou, G. Schuck, Z. Chen, N. Zhang, X. Liu, *Nat. Commun.* **2022**, *13*, 1123.
[19] J. Jin, Y. Liu, X. Zhao, H. Liu, S. Deng, Q. Shen, Y. Hou, H. Qi, X. Xing, L. Jiao, J. Chen, *Angew. Chem., Int. Ed.* **2023**, *62*, 202219230.
[20] G.-L. Xu, X. Liu, X. Zhou, C. Zhao, I. Hwang, A. Daali, Z. Yang, Y. Ren, C.-J. Sun, Z. Chen, Y. Liu, K. Amine, *Nat. Commun.* **2022**, *13*, 436.
[21] a) Y. Li, X. Li, C. Du, H. Sun, Y. Zhang, Q. Liu, T. Yang, J. Zhao, C. Delmas, S. J. Harris, H. Chen, Q. Huang, Y. Tang, L. Zhang, T. Zhu, J. Huang, *ACS Energy Lett.* **2021**, *6*, 3960; b) D. Eum, S.-O. Park, H.-Y. Jang, Y. Jeon, J.-H. Song, S. Han, K. Kim, K. Kang, *Nat. Mater.* **2024**, *23*, 1093.
[22] Z. Dai, Z. Li, R. Chen, F. Wu, L. Li, *Nat. Commun.* **2023**, *14*, 8087.
[23] J. Bao, X. Zhang, B. Fan, J. Zhang, M. Zhou, W. Yang, X. Hu, H. Wang, B. Pan, Y. Xie, *Angew. Chem., Int. Ed.* **2015**, *54*, 7399.
[24] L. Sun, Z. Wu, M. Hou, Y. Ni, H. Sun, P. Jiao, H. Li, W. Zhang, L. Zhang, K. Zhang, F. Cheng, J. Chen, *Energy Environ. Sci.* **2024**, *17*, 210.
[25] J. M. Paulsen, J. R. Dahn, *Solid State Ionics* **1999**, *126*, 3.
[26] S. Kumakura, Y. Tahara, K. Kubota, K. Chihara, S. Komaba, *Angew. Chem., Int. Ed.* **2016**, *55*, 12760.
[27] a) M. H. Han, E. Gonzalo, N. Sharma, J. M. L. d. Amo, M. Armand, M. Avdeev, J. S. Garitaonandia, T. J. C. o. M. Rojo, **2016**, *28*, 106; b) J. Deng, W.-B. Luo, X. Lu, Q. Yao, Z. Wang, H.-K. Liu, H. Zhou, S.-X. Dou, *Adv. Energy Mater.* **2018**, *8*, 1701610; c) G. Liu, W. Xu, J. Wu, Y. Li, L. Chen, S. Li, Q. Ren, J. Wang, *J. Energy Chem.* **2023**, *83*, 53; d) J. Chen, L. Li, L. Wu, Q. Yao, H. Yang, Z. Liu, L. Xia, Z. Chen, J. Duan, S. Zhong, *J. Power Sources* **2018**, *406*, 110; e) M. M. Rahman, J. Mao, W. H. Kan, C.-J. Sun, L. Li, Y. Zhang, M. Avdeev, X.-W. Du, F. Lin, *ACS Mater. Lett.* **2019**, *1*, 573; f) Z. Liu, J. Wu, J. Zeng, F. Li, C. Peng, D. Xue, M. Zhu, J. Liu, *Adv. Energy Mater.* **2023**, *13*, 2301471; g) E. Talaie, V. Duffort, H. L. Smith, B. Fultz, L. F. Nazar, *Energy Environ. Sci.* **2015**, *8*, 2512; h) E. de la Llave, E. Talaie, E. Levi, P. K. Nayak, M. Dixit, P. T. Rao, P. Hartmann, F. Chesneau, D. T. Major, M. Greenstein, D. Aurbach, L. F. Nazar, *Chem. Mater.* **2016**, *28*, 9064; i) Q. Wang, D. Zhou, C. Zhao, J. Wang, H. Guo, L. Wang, Z. Yao, D. Wong, G. Schuck, X. Bai, J. Lu, M. Wagemaker, *Nat. Sustain.* **2024**, *7*, 338; j) Y. You, S. Xin, H. Y. Asl, W. Li, P.-F. Wang, Y.-G. Guo, A. Manthiram, *Chem* **2018**, *4*, 2124; k) C. Zhao, F. Ding, Y. Lu, L. Chen, Y.-S. Hu, *Angew. Chem., Int. Ed.* **2020**, *59*, 264; l) J. Gao, Y. Tian, L. Ni, B. Wang, K. Zou, Y. Yang, Y. Wang, C. E. Banks, D. Zhang, K. Zhou, H. Liu, W. Deng, G. Zou, H. Hou, X. Ji, *Energy & Environmental Materials* **2024**, *7*, 12485; m) H. Zhang, Y. Gao, J. Peng, Y. Fan, L. Zhao, L. Li, Y. Xiao, W. K. Pang, J. Wang, S.-L.

Chou, *Angew. Chem., Int. Ed.* **2023**, *62*, 202303953; n) B. Lung-Hao Hu, F.-Y. Wu, C.-T. Lin, A. N. Khlobystov, L.-J. Li, *Nat. Commun.* **2013**, *4*, 1687; o) X. Dong, Y. Xu, L. Xiong, X. Sun, Z. Zhang, *J. Power Sources* **2013**, *243*, 78.

[28] a) M. A. Fiddy, A. H. Greenaway, *Nature* **1979**, *281*, 709; b) S.-i. Nishimura, G. Kobayashi, K. Ohoyama, R. Kanno, M. Yashima, A. Yamada, *Nat. Mater.* **2008**, *7*, 707; c) C. Wang, R. Wang, Z. Huang, M. Chu, W. Ji, Z. Chen, T. Zhang, J. Zhai, H. Lu, S. Deng, J. Chen, L. He, T. Liang, F. Wang, J. Wang, Y. Deng, W. Cai, Y. Xiao, *Energy Storage Mater.* **2022**, *44*, 1.

[29] G. Kresse, J. Furthmüller, *Comput. Mater. Sci.* **1996**, *6*, 15.

[30] S. Grimme, *J. Comput. Chem.* **2006**, *27*, 1787.

[31] A. E. Mattsson, R. Armiento, P. A. Schultz, T. R. Mattsson, *Phys. Rev. B* **2006**, *73*, 195123.